# Autofocus-Based Estimation of Penetration Depth and Permittivity of Ice Volumes and Snow Using Single SAR Images

Andreas Benedikter, Marc Rodriguez-Cassola, Felipe Betancourt-Payan, Gerhard Krieger, *Fellow, IEEE*, Alberto Moreira, *Fellow, IEEE*

***Abstract*—An intrinsic challenge in the geophysical interpretation of low-frequency SAR imagery of semi-transparent media, such as ice sheets, is the position ambiguity of the scattering structures within the glacial volume. Commonly tackled by applying interferometric and tomographic techniques, their spaceborne implementation exhibits by orders higher complexity compared to missions relying on single SAR images, making them cost expensive or, in the context of planetary missions, even impossible due to limited navigation capability. Besides, even these sophisticated techniques are commonly biased due to inaccurate permittivity estimates, leading to geometric distortions up to several meters. We present a novel inversion procedure to estimate volume parameters of ice sheets, namely, the depth of the scattering layer within the glacial volume and the dielectric permittivity of the ice, based on single-image single-polarization SAR acquisitions. The information is inherent in the processed SAR data as phase errors on the azimuth signals resulting from uncompensated non-linear propagation of the radar echoes through ice. We suggest a local map-drift autofocus approach to quantify and spatially resolve the phase errors and an inversion model to relate them to the penetration depth and permittivity. Testing the proposed technique using P-band SAR data acquired by DLR's airborne sensor F-SAR during the ARCTIC15 campaign in Greenland shows promising results and good agreement with tomographic products of the analyzed test site.**

***Index Terms*—synthetic aperture radar (SAR), autofocus, tomography, cryosphere, glacier, penetration, depth, permittivity.**

## I. Introduction

SYNTHETIC aperture radar (SAR) is a well established remote sensing technique for the exploration of terrestrial and planetary ice sheets. This outstanding position builds upon several SAR-specific characteristics, such as metric or even sub-metric resolution, large spatial coverage, and operability almost independent of atmospheric conditions and solar illumination. Furthermore, electromagnetic waves with wavelengths in the microwave regime partially penetrate into optical non-transparent natural media, such as snow, ice, sand, dry soil, and vegetation. Considering snow and ice environments, that are the focus of this study, this characteristic provides sensitivity of the SAR acquisition to both surface backscatter and scattering phenomena within the snow/ice sheet. Signal backscatter is expected to arise from: i) interfaces separating regions with dielectric contrast, e.g., air/snow, snow/ice, ice/water, and ice/bedrock, ii) ice inclusions in form of volumetric scattering, and iii) subsurface ice layers. This gives access to information about the vertical structure of ice sheets, which, in the terrestrial context, is of fundamental importance for glacier mass balance and dynamics and to gain understanding about the interrelation between the ice masses and environmental processes such as climate change [1], [2]. In the context of planetary exploration, the characterization of the internal structure of planetary ice sheets is a major element in understanding the geology and geophysical processes of planetary bodies and has been pioneered by the exploration of the Martian polar caps [3], [4]. With the rising scientific interest in the active icy moons such as Saturn's Enceladus and Jupiter's Europa, modalities for planetary subsurface ice exploration may play a central role in future missions.

In situ ground-penetrating radar sensors or airborne ice sounding radars are most frequently used for measuring the internal structure of terrestrial ice sheets [5]–[7]. For the exploration of the Martian subsurface two radar sounding instruments have been deployed in orbit [8], [9]. Ice sounders allow for the imaging of the ice sheet subsurface along the radar track by operating a low frequency nadir-looking radar at low altitude. They offer a particular sensitivity to specular scattering occurring at interfaces such as at the bedrock and internal ice layers, providing information on the thickness of the layers. The application of ice sounders is restricted by the limited coverage and backscattering profile estimation owing to the nadir-looking imaging geometry, not allowing for 3-D measurement of the ice sheet. In contrast, the side-looking geometry of spaceborne SAR is able to provide global coverage of terrestrial or planetary ice masses on a regular basis. Various experimental studies have been reported in the literature to overcome the limitation of traditional 2-D SAR imaging, by applying polarimetric and interferometric SAR techniques, allowing for the retrieval of volumetric properties of ice sheets [10]–[12]. Extending the synthetic aperture in elevation direction by multiple acquisitions gathered from slightly displaced radar tracks allows for direct 3-D resolved measurement of ice sheets. This technique is commonly referred to as tomographic SAR (TomoSAR) imaging. TomoSAR allows for the direct retrieval of the vertical ice structure over wide swaths. It

A. Benedikter and G. Krieger are with the Institute of Microwaves and Photonics (LHFT), Friedrich-Alexander University Erlangen-Nürnberg (FAU), 91058 Erlangen, Germany and the Microwaves and Radar Institute, German Aerospace Center (DLR), 82234 Weßling, Germany (e-mail: andreas.benedikter@dlr.de).

M. Rodriguez-Cassola, F. Betancourt-Payan, and A. Moreira are with the Microwaves and Radar Institute, German Aerospace Center (DLR), 82234 Weßling, Germany.

has been successfully applied in several airborne experiments for imaging the internal structure of Alpine glaciers and the Greenland ice sheet [13]–[15] and can be utilized as a robust basis for validation due to its direct 3-D capability.

In this paper, we present an inversion procedure to estimate volume parameters of ice sheets, namely, the depth of the scattering scene within the glacial volume and the dielectric permittivity of the ice, based on a single-image single-polarization SAR acquisition. The information is inherent in the processed SAR data as phase errors on the azimuth signals resulting from uncompensated non-linear propagation of the radar echoes through ice. We suggest a local map-drift autofocus approach to quantify and spatially resolve the phase errors and simple inversion models to relate these errors to the volume parameters. SAR autofocus algorithms have been used over decades to estimate residual platform motion errors [16]–[18] and have been suggested to correct ionospheric-induced phase errors [19], [20], both with the primary goal of recovering the contrast in the SAR image. In the case of a snow/ice scene, besides a corrected radiometry, the measured phase errors can be linked to the underlying physical scene properties, as introduced above. The approach relies on SAR systems with decent Doppler bandwidth to ensure sufficient sensitivity in the phase error measurement. This requirement is met by current airborne sensors such as DLR's F-SAR and spaceborne systems such as TerraSAR-X in staring spotlight mode or ALOS-2 in spotlight mode. The suggested single-image inversion approach may be applied complementary to polarimetric, interferometric, and tomographic imaging, or in applications in which these sophisticated technologies are not implementable such as in planetary missions. We use P-band SAR data acquired by DLR's airborne sensor F-SAR during the ARCTIC15 campaign in Greenland to validate the proposed technique. The considered data consist of repeat-pass acquisitions from the K-transect test site forming a tomographic stack, which will be used to validate the results obtained with the single-image approach.

This paper is organized in six sections. In Section II the problem statement driving the proposed approach is discussed. Section III describes the modelling of the signal propagation, scattering, and resulting phase errors. The concept of the single SAR image inversion approach is presented in Section IV. Results from the airborne data are presented and discussed in Section V. Conclusions are drawn in Section VI.

## II. Problem Statement

An important geophysical distinction of SAR image features in the assessment of ice sheets is their characterization as surface or volume structures and furthermore, their exact position within the ice. The intrinsic difficulty in SAR imaging of semi-transparent media, such as snow or ice, is the ambiguity in the position of the scattering structures within the media, even if the topography of the surface is known. An example of the complex backscatter situation of an ice sheet is illustrated in Figure 1, where different features may contribute to the return signal in a single resolution element which extends in elevation direction and is only bounded by the antenna beam width. This

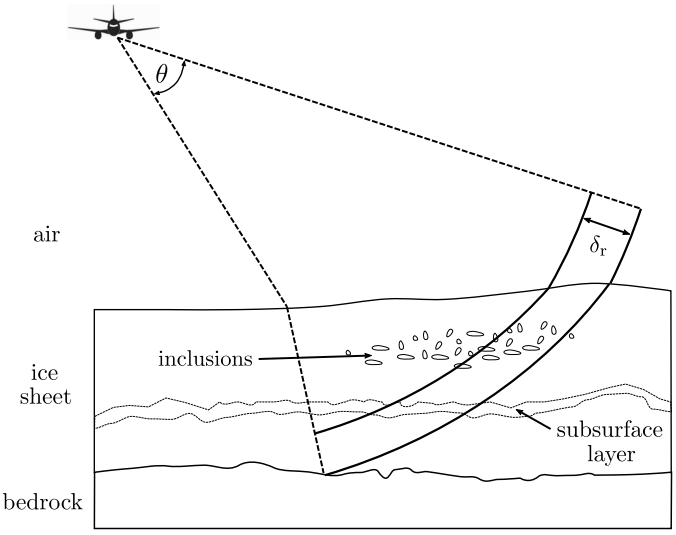


Fig. 1. Illustration of the potentially complex backscatter scenario of an ice sheet. Scattering sources from various depths may contribute in the SAR resolution cell, indicated by the range resolution $\delta_r$ and bounded by the antenna beamwidth $\theta$.

features can reach from the surface to the bedrock underneath the ice.

As introduced above, the elevation ambiguity may be resolved by applying SAR interferometric or tomographic techniques which require the use of several satellites or coherent repeat passes. Although considered standard in the context of Earth observation missions, e.g., TanDEM-X and Sentinel-1, when considering planetary missions, the implementation of interferometric techniques may fail due to exceeding cost and complexity, as well as the limited accuracy in navigation and orbit determination. The stress here on the planetary context is due to the frame out of which this study emerges: a radar mission concept investigation for the exploration of Saturn's ice-covered moon Enceladus [21], where possible spacecraft orbits experience strong perturbation by Saturn's mass and the strongly non-spherical gravity field of Enceladus. Combined with the limited spacecraft navigation accuracy for outer solar system missions, the stringent navigation requirements for interferometric missions are expected to be difficult to meet. This drives the need for the proposed approach to infer the scattering position from single SAR images.

Besides the position of scattering features, the composition, i.e., the density of ice sheets is a significant geophysical parameter as it allows for example to distinguish between snow, firn, and ice. Radar acquisitions are inherently sensitive to the density of a glacial volume as it is directly related to the dielectric permittivity and therefore the propagation velocity of radar signals. This sensitivity may be exploited to obtain permittivity estimates.

Moreover, an accurate permittivity knowledge is crucial for providing reliable interferometric penetration estimates and tomographic acquisitions, as the vertical wavenumber is directly related to it [22]. Permittivity values are commonly only available as rough estimates. Considering tomography, permittivity is commonly incorporated in form of a geometric correction step after tomographic processing assuming free

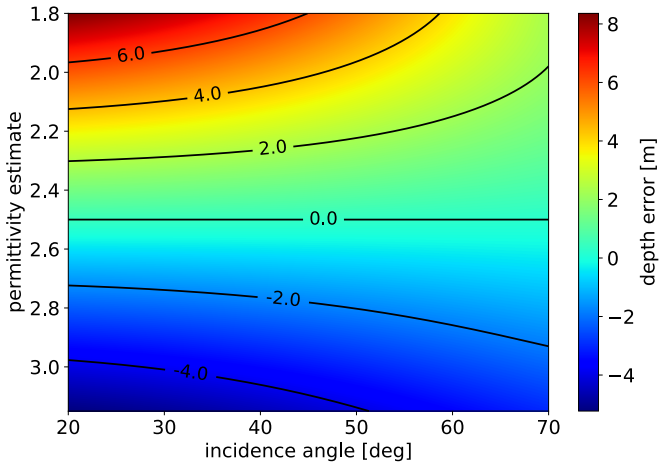


Fig. 2. Error in the estimation of the depth of a target retrieved from a tomographic product caused by inaccurate permittivity estimates. Results are shown for a target located $50\,\mathrm{m}$ deep in an ice sheet with averaged permittivity of 2.5. Positive values indicate an overestimation. Note the dependence with incidence angle on the ice sheet surface.

space propagation [14]. Derived from the relations given in [14], Figure 2 displays the tomographic estimation errors of the depth of a structure located $50\,\mathrm{m}$ deep in an ice sheet with mean permittivity of $2.5$, i.e., a permittivity corresponding to medium dense firn. Errors are analysed for permittivity estimates spanning a range from slightly dense firn (i.e., $1.8$) to solid ice (i.e., $3.15$), and incidence angles on the surface between $20°$ and $70°$. For different depths, the error is varying linearly. Significant errors can be expected in cases where no additional measurements constrain the permittivity range. A further independent approach for penetration estimation, as discussed in this study, can allow for the estimation of the permittivity.

## III. Propagation and Phase Error Model

### A. Propagation and Scattering in Snow and Ice

Considering radar systems operating in commonly used frequency bands, e.g., from P to X, when the radar echo impinges on the interface between air and snow/ice a significant part of the energy is not scattered but penetrates into the glacial volume [23]. The ratio of scattered and penetrating signal energy is dependent on the signal frequency, the dielectric permittivity of the surface layer, and the surface roughness [23]. Low values of these quantities lead to strong signal penetration. The penetrating electromagnetic wave experiences a change in propagation velocity, which, under the assumption of snow and ice as a low-loss material, can be written as [24]

$$c_{\mathrm{ice}} = \frac{c_0}{\sqrt{\varepsilon_{\mathrm{r,ice}}}} = \frac{c_0}{n_{\mathrm{ice}}}, \tag{1}$$

where $c_0$ is the speed of light in free space, $\varepsilon_{\mathrm{r,ice}}$ the real part of the permittivity of snow/ice, and $n_{\mathrm{ice}}$ the corresponding refractive index, which is mainly used throughout the paper, as it eases the description of propagation phenomena. The index *ice* is from here on used to indicate parameters describing the glacial volume. The velocity change results in a direction change of the penetrating wave which can be described using Snell's law of refraction [24]:

$$n_{\mathrm{air}} \cdot \sin\theta_{\mathrm{i}} = n_{\mathrm{ice}} \cdot \sin\theta_{\mathrm{r}}, \tag{2}$$

with $\theta_{\mathrm{i}}$ being the incident angle of the echo at a surface point with respect to the surface normal and $\theta_{\mathrm{r}}$ the refraction angle.

Within the glacial volume the propagating signal may be backscattered by volumetric distributed inclusions, such as air inclusions, ice lenses and pipes, and depth hoar, in form of volume scattering. Furthermore, backscatter occurs in form of surface scattering at interfaces separating layers with dielectric contrast, i.e., snow/firn, snow/ice, water bodies, refrozen wet snow or firn, and glacier/bedrock. Along its propagation path, the signal experiences an attenuation which results from scattering and dielectric absorption losses. Both processes increase with higher frequencies. In P and L bands, commonly used for ice-penetrating SAR systems, ice sheets are relatively transparent when compared to other natural media and studies record backscatter signatures in SAR acquisitions down to several tens of meters [13]–[15]. Above two GHz the absorption losses rise drastically due to increasing dielectric losses, represented by the imaginary part of the permittivity. Besides, the scattering losses show a strong dependence on the frequency, commonly modeled with a $f^4$ proportionality [25]. The propagation velocity within the glacial volume changes according to (1) with the refractive index, which can be assumed to be frequency independent in the microwave region with a slight temperature dependence [26]. The value for $n_{\mathrm{ice}}$ of pure ice is typically assumed to be around $\sqrt{3.15}$ [27]. However, the $n_{\mathrm{ice}}$ of snow and firn strongly depends on its density and water content. Assuming cold conditions, ice sheets are commonly modeled as a with-depth-increasing density, leading to an equivalent $n_{\mathrm{ice}}$ profile with common starting values for snow of about $\sqrt{1.4}$ [27] and saturating at the refractive index of pure ice. Real ice sheets may exhibit more complex refractive index distributions, especially in regions where melting and refreezing events lead to strongly heterogeneous density distributions, e.g., highly reflecting layers.

The travel path of the radar echoes in complex $n_{\mathrm{ice}}$ distributions is non-linear and can be approximated by Fermat's principle of least time, which states that the path of a ray taken between two points in an arbitrary heterogeneous medium is the one for which the ray takes the least time compared to adjacent paths [24]. The approximation made is to treat the travelling wave as propagating rays which are perpendicular to the wave fronts. It is almost perfect if the wavelength is small compared to the structures with which it interacts, but it cannot account for effects like diffraction and interference [24]. Also Snell's law in (2) is subject to this high-frequency approximation. Generally speaking, the authors see the approximation applicable for ice-penetrating radar applications, as the small scale variations within the glacial volume, i.e., the conglomerate of ice particles and air, are sufficiently small compared to radar wavelengths to be assumed homogeneous, whereas the interfaces between layers and permittivity profiles vary in large spatial extents compared to radar wavelengths. The validity of the approximation may

be proven wrong if wavelength sized structures are present, such as ice lenses or pipes. Nonetheless, it is an indispensable tool for approximating the travel time and path of the radar echoes through the glacial volume and is frequently used in the community.

### B. SAR Signal Model

The received SAR signal echoed from a point target after demodulation can be modelled as [28]

$$s_{\mathrm{rx}}(t,t_{\mathrm{a}}) = \mathrm{rect}\left[\frac{t-\tau(t_{\mathrm{a}})}{\tau_{\mathrm{p}}}\right]\cdot\exp\left[\mathrm{j}\cdot\pi k_{\mathrm{r}}\cdot\left(t-\tau(t_{\mathrm{a}})\right)^2\right] \cdot w^2\left(t_{\mathrm{a}}\right)\cdot\exp\left[-\mathrm{j}\cdot 2\cdot\pi\cdot f\cdot\tau(t_{\mathrm{a}})\right], \quad (3)$$

where $t$ is the slant range time, $t_{\mathrm{a}}$ the azimuth time, $\tau_{\mathrm{p}}$ the pulse duration, $k_{\mathrm{r}}$ the chirp rate, $w\left(t_{\mathrm{a}}\right)$ the illumination footprint of the antenna over the scene, and $\tau(t_{\mathrm{a}})$ the variation of the two-way travel time to the target along azimuth, which is referred to as travel time history from here on. The backscatter coefficient of the target is set to unity. The signal model is equivalently applicable for conventional SAR acquisitions assuming free space propagation and for subsurface imaging through a dielectric heterogeneous propagation medium such as ice. The only difference lies in the formation of the travel time history, further discussed below. If not considering a discrete point target but a complex glacial volume as backscattering source, as depicted in Figure 1, the return of all targets within the resolution cell integrates into the echo. The resolution cell extends in elevation direction and is only bounded by the antenna beam width, leading to a superposition of backscatter sources from different depths through the ice sheet. Commonly, the signal is dominated by specific scattering sources. For P-band and L-band frequencies, subsurface scattering often contributes the strongest returns, whereas at higher frequencies, the backscatter arises mainly at the surface. For conventional SAR imaging, the vertical position of the scattering source is not accessible.

SAR data are commonly processed assuming free-space propagation between radar and target allowing for a trivial computation of the travel time history and therefore the phase history. For a target located within an ice sheet, $\tau(t_{\mathrm{a}})$ experiences additional influence by the change in propagation velocity and travel path non-linearity, according to the relations discussed in Subsection III-A. The resulting mismatch between the processing kernel and the phase history of the target leads to defocusing in the processed SAR image depending on the magnitude and shape of the phase error history. Commonly perceived as an undesired effect, the defocusing may be exploited to gain information about the ice permittivity and target depth, if precisely measured and modelled.

The acquisition geometry for a simplified scenario with a linear radar track, a flat interface between air and the ice sheet, and a constant refractive index $n_{\mathrm{ice}}$ is illustrated in Figure 3, where the refraction on the surface leads to a non-linear travel path of the echoes. For a target located within an ice sheet the derivation of the travel time history and therefore the phase history is non-trivial. Even for the simple scenario in Figure 3, a closed form expression is not possible, as the

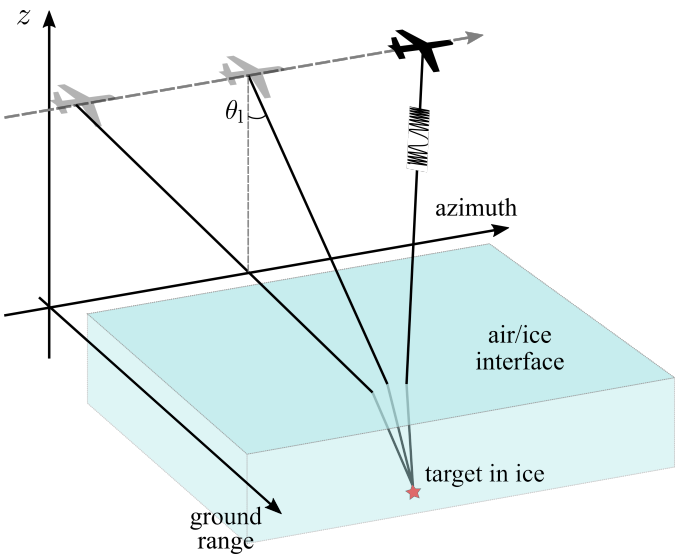


Fig. 3. Simplified acquisition geometry for a target located within an ice sheet of constant refractive index and flat surface, illustrating the refraction effect on the ice surface.

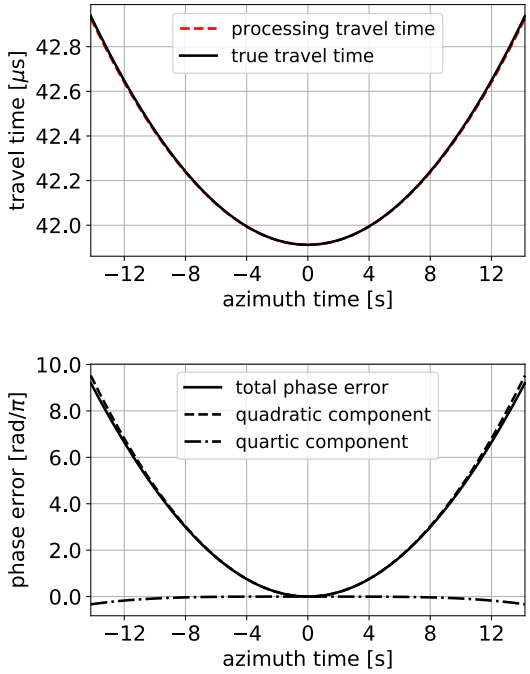


Fig. 4. (Top) simulated travel time history for a target located $50\,\mathrm{m}$ deep in an ice sheet of refractive index $\sqrt{3.1}$ according to F-SAR acquisition parameters in Table II in black, compared to the travel time history used for processing assuming free space in dashed red. (Bottom) phase error between the two histories and its quadratic and quartic component.

derivation of the travel time along a single ray path requires the computation of the intercept point on the surface, leading to the determination of the roots of a fourth-order polynomial [29], which results in unpractical analytical expressions.

*1) Phase Error Simulation:* The simulated travel time history for a point target located $50\,\mathrm{m}$ deep in ice is shown in Figure 4 (upper panel) and is compared to a target at the same slant range time in a free space surrounding, i.e., the

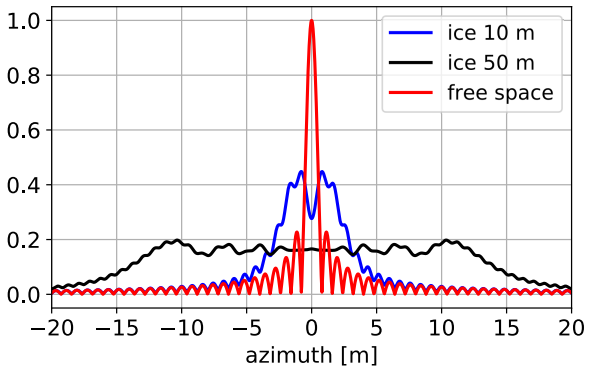


Fig. 5. Simulated azimuth IRF of a target located 10 m and 50 m deep in an ice sheet with a refractive index of $\sqrt{3.1}$, processed assuming free space propagation and compared to a target at equivalent slant range time located in free space. F-SAR P-band acquisition parameters are used for the simulation, depicted in Table II. Note the strong defocusing, even for the target at 10 m depth.

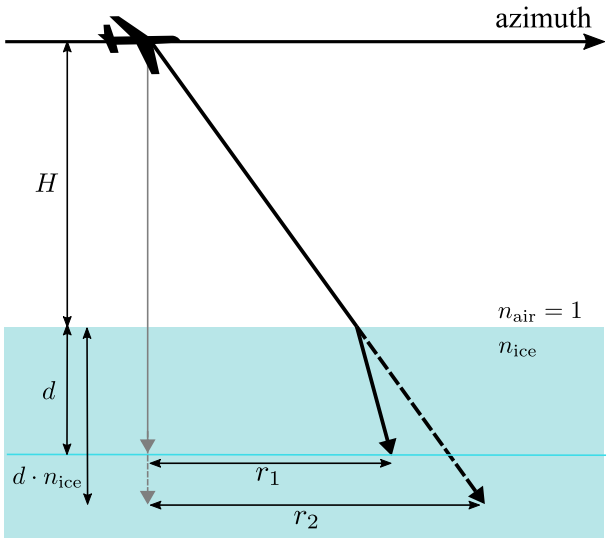


Fig. 6. Geometric relations for the derivation of the Doppler rate.

assumption made in processing. The simulation geometry is comparable to the one in Figure 3 with a constant refractive index $n_{\text{ice}} = \sqrt{3.1}$ and an incidence angle on ice of 50°. System parameters such as sensor altitude, frequency, and integration time are chosen according to the analyzed data in Section V of the F-SAR flight campaign and listed in Table II. The computation of travel times was performed using a numerical minimization according to Fermat's principle. The difference between the two travel time histories is shown in the lower panel of Figure 4 in form of a phase error describing the difference between the two corresponding phase histories. Furthermore, the two most significant polynomial terms of the phase error, i.e. the quadratic and quartic component, are derived from an order-ten polynomial fit. The hyperbolic appearance of the phase error is well described by its quadratic component, even for the relatively large Doppler bandwidth of the F-SAR P-band acquisition. At the boarders of the synthetic aperture a maximum phase error of $\approx 9.1\pi$ is reached. The effect of the phase error on the azimuth impulse response function (IRF) is depicted in Figure 5 for a target 50 m deep in ice (corresponds to results in Figure 4) and 10 m deep. The IRFs are compared to the one of a target located at the same slant range time but in free space, which appears well focused. The severe phase errors lead to a heavy defocusing of the IRF even for the target located 10 meters under ice. This effect for subsurface SAR imaging of ice sheets has also been mentioned in [14], but regarded as negligible for the processed azimuth resolution of five meters. For finer nominal azimuth resolution, as in the present data set, the phase error cannot be neglected and increases proportional to $1/\delta_{\text{a}}^2$, with $\delta_{\text{a}}$ being the azimuth resolution. In [30] it is shown that for very fine azimuth resolution (i.e., $< 0.5$ m in P-band) the defocusing effect may be even exploited to obtain a 3-D metric resolution effect.

*2) Phase Error Model:* As outlined in the discussion of Figure 4, the phase error is well described by its quadratic component. This facilitates to approximate the phase history by an order-two polynomial. For non-squinted acquisitions the phase history may be approximated as [28]

$$\Phi(t_{\text{a}}) \approx \tau_0 \cdot f \cdot 2 \cdot \pi + f_{\text{R}} \cdot \pi \cdot t_{\text{a}}^2, \tag{4}$$

where $\tau_0$ is the minimum of the travel time history and $f_{\text{R}}$ is the Doppler rate. From a target's perspective, the Doppler rate describes the changing rate of Doppler frequency under which it is observed. For a target in free space it is given by [28]

$$f_{\text{R, fs}} = \frac{4 \cdot v_{\text{e}}^2}{\lambda_0 \cdot c_0 \cdot \tau_0}, \tag{5}$$

with $\lambda_0$ being the wavelength in free space and $v_{\text{e}}$ the effective velocity between sensor and target. A target located in ice perceives a faster changing Doppler frequency due to a compacting of the azimuth sampling and therefore a higher Doppler rate. The Doppler rate may be derived by quantifying the compacting. In Figure 6 the distance between two Doppler frequency samples for a depth $d$ in the ice is illustrated for the actual case of $n_{\text{ice}} > n_{\text{air}}$ and $n_{\text{ice}} = n_{\text{air}}$, $r_1$ and $r_2$, respectively. For the latter case, $d$ is scaled with $n_{\text{ice}}$ to account for the higher propagation velocity. The ratio $\frac{r_2}{r_1}$ relates the Doppler rate for a target in ice to the Doppler rate of a free space assumption, i.e., the Doppler rate used in processing:

$$f_{\text{R}} = f_{\text{R, fs}} \cdot \frac{r_2}{r_1} = f_{\text{R, fs}} \cdot \zeta, \tag{6}$$

where $\zeta$ is used from here on as a short hand notation. For deriving $\zeta$, the side-looking geometry and refraction in the slant range plane have to be taken into account, resulting in

$$\zeta \simeq \frac{\left(H + d \cdot n_{\text{ice}} \cdot \frac{\cos\theta_{\text{i}}}{\cos\theta_{\text{r}}}\right) \cdot n_{\text{ice}}}{H \cdot n_{\text{ice}} + d \cdot \frac{\cos\theta_{\text{i}}}{\cos\theta_{\text{r}}}}, \tag{7}$$

where $H$ is the sensor altitude and $\theta_{\text{i}}$ and $\theta_{\text{r}}$ are the incidence and refraction angle in the slant range plane at boresight. Following, the phase error can be modelled as

$$\Delta\Phi(t_{\text{a}}) = f_{\text{R, fs}} \cdot \pi \left(\zeta - 1\right) \cdot t_{\text{a}}^2. \tag{8}$$

Together with the derived model parameter in (7), the expression in (8) provides an estimation of the phase error to

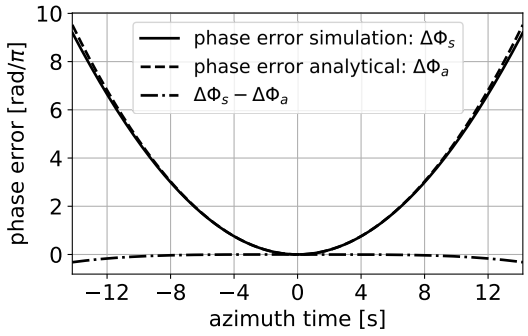


Fig. 7. Comparison of the simulated phase error history according to Figure 4 and the analytical expression in (8).

be expected for targets located in an ice sheet of constant refractive index when the processing of the data is performed under the common assumption of free space propagation. The model is used in the following sections as inversion model for estimating the depth of an imaged feature $d$ and the refractive index of the ice sheet $n_{\text{ice}}$. To validate the phase error model, in Figure 7 the analytical expression of (8) is used to replicate the phase error from the analysis of Figure 4. Obviously, the analytical expression only accounts for the quadratic component, leaving a quartic component after forming the difference.

*3) Discussion:* The derived relations allow for a simple modeling of the quadratic phase error induced by the propagation of the echoes through ice. For realistic acquisition scenarios, violating the flat Earth assumption in the derivation of the model, the topography can be locally approximated by tangential planes. This approximation holds under the assumption that the topography is varying insignificantly within the area where the echoes of a target impinge on the glacial surface. Considering realistic penetration depths down to $100\,\text{m}$, this area extends in the order of tens of meters, making the approximation tolerable in a wide range of cryospheric application scenarios. The accommodation of realistic refractive index distributions follows a similar rationale. A distribution that is laterally varying insignificantly within the spatial extent spanned by the echo ray paths may be approximated by a constant refractive index even if heterogeneous in vertical dimension. Errors in both approximations result in linear and higher-order phase terms additional to the modelled quadratic term.

The expression in (8) is used in Figure 8 to model the maximum quadratic phase error for a wide span of target depths and refractive indices, with the maximum error located at the borders of the synthetic aperture. In the upper panel, system parameters correspond to the F-SAR P-band acquisition depicted in Table II with an incident angle on the surface of $50°$. The $0.25\pi$ contour (red) marks the phase error that is commonly regarded as the limit at which a visual degradation of the SAR image starts and is also frequently stated as an empirical estimation of the accuracy limit of autofocus algorithms. For the F-SAR parameters, almost all constellations in the analyzed parameter space surpass this border. The lower panel of Figure 8 displays for TerraSAR-X staring spotlight system parameters, depicted in Table I, that significant phase errors can be expected even with the limited penetration expected for X-band signals, if sufficient Doppler bandwidth is available. Computations were performed assuming a spherical Earth approximated by a tangential plane at the point of incidence.

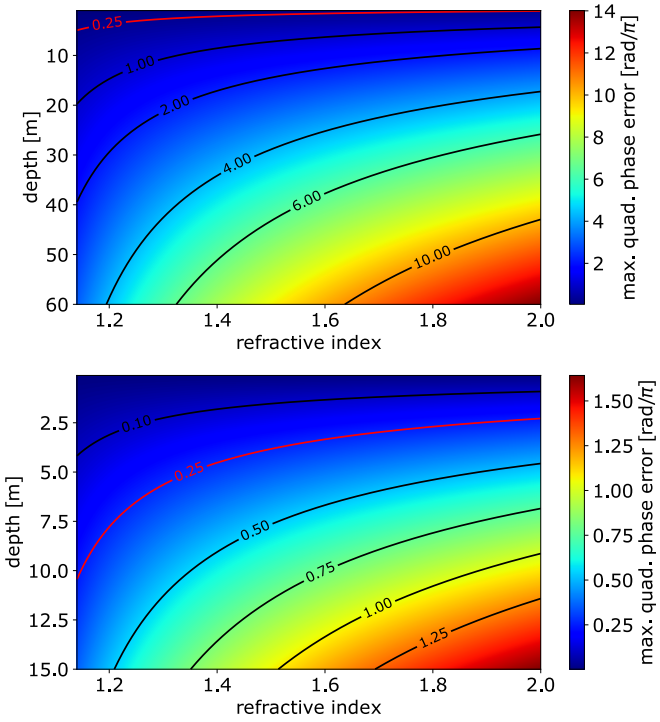


Fig. 8. Maximum quadratic phase error between the correct phase history of a target located in an ice sheet and the phase history of the processing kernel (assuming free space) for varying refractive indices and target depths. (Top) acquisition parameters chosen according to the F-SAR P-band data depicted in Table II and (bottom) parameters according to TerraSAR-X staring spotlight depicted in Table I.

TABLE I
EXEMPLARY TERRASAR-X STARING SPOTLIGHT ACQUISITION PARAMETERS

| **Parameter** | **Value** |
|---|---|
| Center frequency | $9.65\,\text{GHz}$ |
| Processed azimuth resolution | $0.24\,\text{m}$ |
| Sensor altitude | $514\,\text{km}$ |
| Incidence angle | $50°$ |

## IV. INVERSION APPROACH

Inverting the penetration and permittivity from the phase error present in SAR images necessarily follows a three-stage approach:

1) SAR processing,
2) phase error estimation via autofocus algorithm,
3) inversion of phase errors.

The general procedure of the single-image inversion approach is depicted in Figure 9. The first stage, SAR processing, describes conventional SAR focusing of the acquired raw data assuming free space propagation. One preliminary assumption

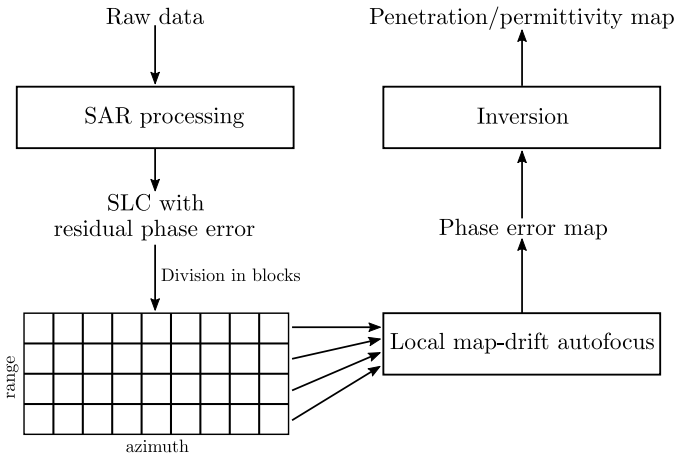


Fig. 9. Block diagram of the proposed single-image inversion approach. Note that the blocks are treated separately in the local map-drift autofocus.

of the approach is that nominal calibration has already been applied on the data, to make sure most of the residual phase signatures are due to the propagation within the volumes of interest. In a second stage, phase errors are estimated using a SAR autofocus algorithm, namely, a local map-drift autofocus applied on the focused single-look complex SAR image (SLC). The autofocus is applied block-wise on the focused data, resulting in a spatially-resolved phase error map over the imaged scene. Finally, the estimated phase errors are fed into an inversion model based on the results presented in Section III, which allows the generation of penetration maps or permittivity estimates.

### *A. Local Map-Drift Autofocus*

SAR autofocus approaches are broadly used for the estimation and correction of phase errors to produce high-resolution SAR imagery. The two most commonly applied approaches are the phase gradient autofocus (PGA) and the map-drift autofocus (MDA) [16]. PGA allows for the estimation of arbitrary phase error functions [17], but the necessity of bright, point-like targets restricts the applicability for glacial terrain. Moreover, as the aim of the suggested approach is to estimate and invert scene-induced phase errors, point-like features would need to be well distributed over the scene. Therefore, an MDA method is preferred, which requires only the presence of contrast features in the scene, such as edges, shadows, and other details. Contrast may be found in subsurface glacial scenes in the form of bed rock reflection or reflection from volume structures. MDA, in its basic form, estimates the second derivative of the phase error function by measuring a linear shift between two images generated from two azimuth sublooks [16]. When considering a phase error dominated by a quadratic term -as described above-, the second derivative is proportional to the error in Doppler rate $\Delta f_{\mathrm{R}}$ between the processing kernel and the actual phase history, which has been shown in Section III to be roughly proportional to the penetration depth and the permittivity of the volume. This becomes evident by taking a look at the phase history formulation in (4).

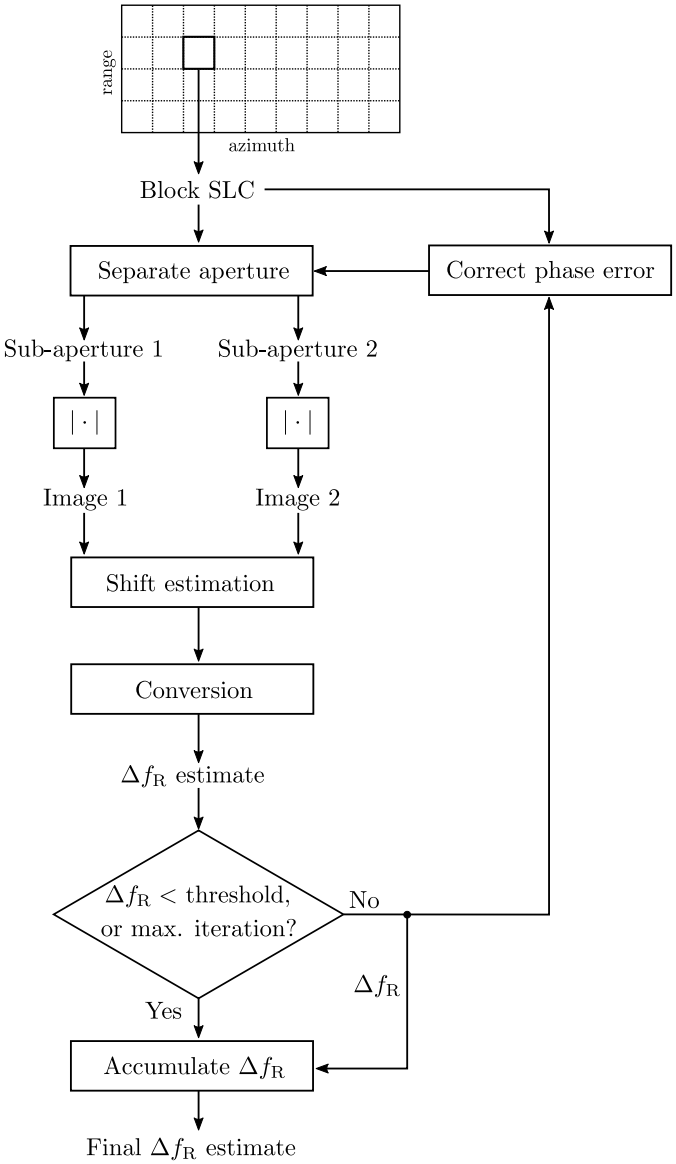


Fig. 10. Block diagram of the local map-drift approach.

In Figure 10, the basic steps of the developed MDA method are displayed. The autofocus is applied in blocks to get local estimates of the propagation errros. For every block, the shift between the amplitude images generated from the two azimuth sublooks is estimated using a 2-D cross-correlation. Sub-pixel accuracy is reached by evaluating the slope of the phase of the cross-correlation spectrum, with the slope being connected to the shift of the cross-correlation peak over Fourier theorems. When considering the images formed from two equally-sized, non-overlapping sublooks spanning together the whole aperture, the azimuth pixel shift $\Delta x$ can be related to the Doppler rate error over [31]

$$\Delta f_{\mathrm{R}} = \frac{2 \cdot \Delta x}{B_{\mathrm{D}}^2 \cdot \mathrm{osf}} \cdot f_{\mathrm{R,proc}}^2, \tag{9}$$

where $B_{\mathrm{D}}$ stands for the Doppler bandwidth, osf is the oversampling factor, and $f_{\mathrm{R,proc}}$ describes the Doppler rate used for processing. The MDA is applied in an iterative manner, in

which the estimated $\Delta f_{\mathrm{R}}$ after each iteration is used to correct the quadratic phase error in the spectrum of the block SLC. Typically, this leads to an improvement of the $\Delta f_{\mathrm{R}}$ estimate, because each correction step leads to a contrast enhancement in the image, allowing a higher-accuracy shift measurement. In each iteration k, $f_{\mathrm{R,proc}}$ is updated according to

$$f_{\mathrm{R,proc;\,k}} = f_{\mathrm{R,proc;\,k\text{-}1}} + \Delta f_{\mathrm{R;\,k\text{-}1}} \tag{10}$$

and $\Delta f_{\mathrm{R}}$ is accumulated to obtain the total Doppler rate error. The process is terminated when $\Delta f_{\mathrm{R}}$ reaches a lower threshold, or after a maximum number of iterations. Commonly, after two or three iterations of corrections, the measurement converges and does not improve further. Each block is treated separately and the Doppler rate error is assumed constant over the block. The initial value of $f_{\mathrm{R,proc}}$ is calculated according to (5) at mid-range of the considered block. For a thorough description of the particularities and implementation of the map-drift algorithm the reader is referred to Carrara et al. [16].

### B. Inversion

Based on the error model presented in Section III, we can relate the output of the autofocus to the penetration and the permittivity of the ice volume. According to (6) the model parameter $\zeta$ can be estimated as

$$\zeta = 1 + \frac{\Delta f_{\mathrm{R}}}{f_{\mathrm{R,\,fs}}}. \tag{11}$$

Therefrom, based on (7) the depth of the dominantly scattering scene (i.e., the penetration depth) $d$ is expressed as

$$d = \frac{n_{\mathrm{ice}} \cdot (H - H \cdot \zeta)}{\frac{\cos\theta_{\mathrm{i}}}{\cos\theta_{\mathrm{r}}} \cdot (\zeta - n_{\mathrm{ice}}^2)}. \tag{12}$$

For obtaining the refractive index $n_{\mathrm{ice}}$, the refraction angle $\theta_{\mathrm{r}}$ in (7) has to be expressed according to Snell's law. Solving for $n_{\mathrm{ice}}$ results in four roots of which only one takes physical values and has the form

$$n_{\mathrm{ice}} = \sqrt{\frac{-b + \sqrt{b^2 - 4 \cdot a \cdot c}}{2 \cdot a}}, \tag{13}$$

with

$$a = \cos^2(\theta_{\mathrm{i}}) \cdot d^2, \tag{14}$$

$$b = -2 \cdot \zeta \cdot \cos^2(\theta_{\mathrm{i}}) \cdot d^2 - H^2 \cdot (1-\zeta)^2, \text{ and} \tag{15}$$

$$c = \cos^2(\theta_{\mathrm{i}}) \cdot d^2 \cdot \zeta^2 + \sin^2(\theta_{\mathrm{i}}) \cdot H^2 \cdot (1-\zeta)^2. \tag{16}$$

The dependence of the phase error to both, the depth and the refractive index does not allow for the joint estimation of both parameters from a single acquisition. Previous knowledge of one of them or additional acquisitions are required.

*1) Single Image Inversion:* Considering a single SAR image being the only available measurement, a penetration depth inversion according to (12) is the primary application scenario of the inversion approach as the refractive index of a snow and ice sheet may be bound to a certain range depending on weather conditions and geographic location. The sensitivity of the penetration inversion to errors in the refractive index (i.e., permittivity) knowledge is shown in Figure 11 for the example

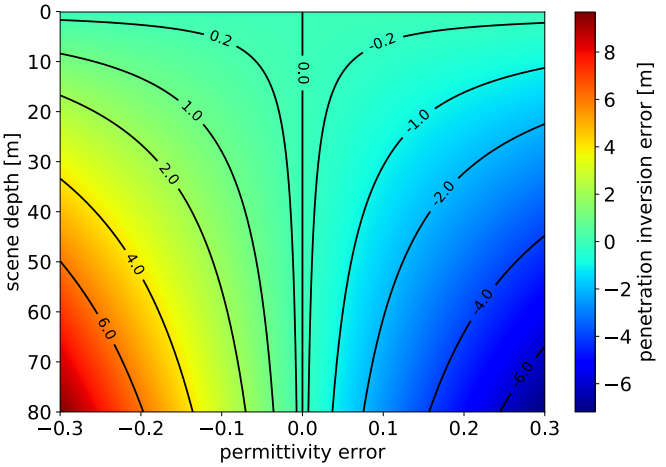


Fig. 11. Error in the penetration depth inversion using the single-image approach resulting from errors in the permittivity knowledge, shown for the F-SAR acquisition geometry, different depths of the scattering scene within the ice sheet, an incident angle on the surface of 45°, and an exemplary true permittivity of the ice sheet of 2.5.

case of an ice sheet with mean permittivity of 2.5, corresponding to medium dense firn. The results are shown for the F-SAR acquisition geometry with a sensor altitude of 4000 m, different depths of the scattering scene within the ice sheet, and an incident angle on the surface of 45°. For penetration depths in the range of several tens of meters, as expected for example in P-band, and representative permittivity error magnitudes up to 0.3, inversion errors with magnitudes up to few meters are to be expected. Note that the sensitivity to permittivity errors of the single-image approach is higher compared to interferometric or tomographic techniques. However, the magnitude of the analysed penetration errors does not seem to drastically limit the usability for the exploration of ice sheets. Note also that permittivity distributions within ice sheets may exhibit a significant vertical heterogeneity, as introduced in Subsection III-A. Such permittivity profiles can be naturally incorporated in form of an effective constant permittivity if an estimate of the vertical profile is available.

For a refractive index inversion, hardly any bound can be put on an estimate of the penetration depth. Additional in situ measurements are required to constrain the expected penetration.

*2) Multiple Image Inversion:* If more than one SAR image with different aspect angles on the scene are available, the geometric diversity may be exploited to jointly estimate the penetration and permittivity. At this point the potential of a joint estimation using the single-image approach and the information from multiple acquisitions is outlined briefly. A dedicated assessment is left for future research.

Considering coherent acquisitions in form of SAR interferometry or tomography, the single-image approach may be used to calibrate the refractive index estimate to obtain unbiased penetration estimates and tomographic imaging. The calibration relies on the above introduced property that interferometry and tomography exhibit a different sensitivity to permittivity errors than the single-image approach, leading to

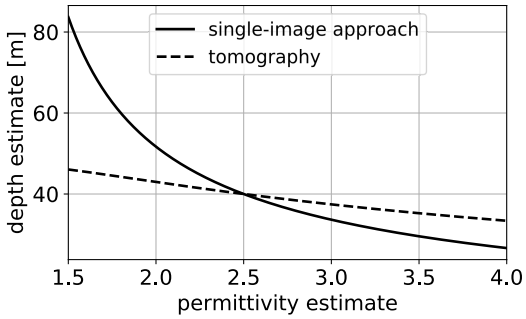


Fig. 12. Depth estimate for erroneous permittivity estimates for a target located 40 m deep in firn of permittivity 2.5, comparing the single-image approach and tomographic products. Note the difference in the sensitivity to the permittivity errors.

diverging depth estimates for erroneous permittivity estimates. This characteristic is displayed in Figure 12, comparing the depth estimate of a target using permittivity corrected tomography and the single-image approach. The target is located in firn of permittivity 2.5 at a depth of 40 m acquired with an incidence angle of 50°. Results are shown for a wide span of permittivity estimates. The correct permittivity can be calibrated according to the best agreement between the two estimates. The calibration is unambiguous but is limited by the accuracy of the two measurements.

Besides coherent acquisitions, repeat-pass acquisitions with large baselines may be exploited to jointly solve the system of depth and permittivity by additionally evaluating the range shift of subsurface image features between the geometrically co-registered acquisitions. The range shift is a consequence of the sensitivity of the refraction effect to the incidence angle on the ice surface.

## V. Validation With F-SAR Data

### A. Experimental Data

The experimental dataset utilized in this study was acquired in May 2015 in the frame of the ARCTIC15 campaign by DLR's airborne sensor F-SAR [32]. The test site is the K-transect in South-West Greenland (67°4′ N, 49°23′ W) and its location is depicted in Figure 13. The analysed data are multi-baseline, fully polarimetric P-band acquisitions over approximately 100 km with a swath of 3 km from the west coast to the inner part of the ablation zone of the ice sheet. The campaign consisted of 8 parallel flight tracks at an altitude of approximately 4000 m with a maximum horizontal separation of 270 m. The acquisition parameters are depicted in Table II. A single-pass X-band digital elevation model (DEM) was acquired and used for processing and geocoding. The DEM is referenced to corner reflectors on the ice sheet surface. Topography dependent, navigation based motion compensation was carried out during processing.

The imaged area is part of the ablation zone of the glacier consisting of solid glacier ice covered with a dry snow layer [33]. An ice-free (i.e., surface) section is located on the left side of the images. Only few snow and ice fields are scattered in this area. The test site was chosen for the present study due


Fig. 13. Location of the K-transect test site in South-West Greenland (67°4′ N, 49°23′ W).

TABLE II
F-SAR P-band Acquisition Parameters

| Parameter | Value |
|---|---|
| Center frequency | 435 MHz |
| Processed azimuth resolution | 1.0 m |
| Processed range resolution | 3.84 m |
| Sensor altitude | 4000 m |
| Incidence angle range | 25° to 60° |

to its large spatial extent, the predictable refractive index of solid ice, and the transition between ice-free terrain and the ice sheet. An overview on the imaged scene and first insight in the scattering behaviour is provided by the quick looks in Figure 14, showing an amplitude image in HH polarization and a polarimetric decomposition, i.e., Figure 14a and 14b, respectively. On the left hand side of the swath, the ice-free section is located. The ice covered area, taking the largest part of the scene, may be roughly distinguished into two different backscatter behaviours. A SAR tomographic analysis of the test site in [34] displays that the dark regions in the amplitude image, corresponding to the blue colored areas in the Pauli image, are dominated by scattering from near surface layers, whereas the bright areas, i.e., green colored, can be attributed to volumetric scattering from subsurface layers.

### B. Penetration Inversion Using the Single-Image Approach

For simplicity reasons, a rectangular crop of the imaged scene is utilized to test the single-image approach. The image crop extends 2.5 km in range and 100 km in azimuth and is shown in in Figure 15a. HV polarization is chosen, due to the high sensitivity to volumetric scattering and therefore enhanced probability for subsurface features dominating the backscatter. The local map-drift approach is applied in a block-wise manner on the processed data. Blocks have a size of 2048 x 256 samples in azimuth and range, respectively. The choice of block size is a trade-off between spatial resolution


(a)

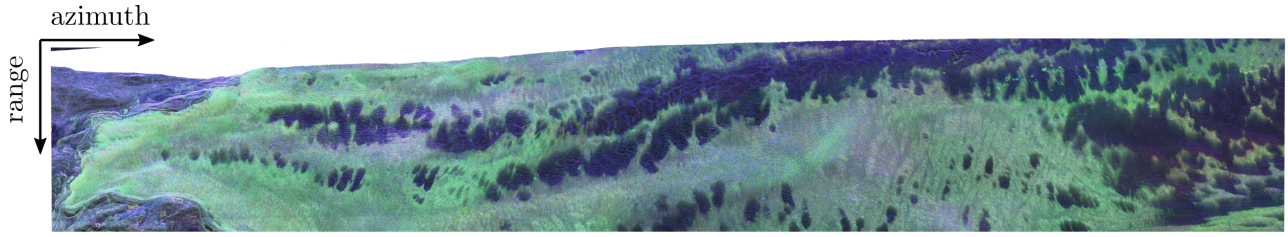


(b)

Fig. 14. (a) P-band amplitude image of the K-transect scene in HH polarization. (b) Pauli polarimetric decomposition of the scene. The blue color indicates a backscatter behaviour dominated by surface scattering and the green color indicates dominant volume scattering.

and accuracy, or rather reliability, of the measurement. A block needs to be sufficiently large to contain enough contrast features for the cross-correlation to provide reliable shift estimates. Especially in the low-contrast case of an ice sheet, relatively large blocks have to be used. The sensitivity of the cross-correlation to low-amplitude features is strengthened by applying it on the square-root of the amplitude image. In order to track the changes of the autofocus estimates, $90\,\%$ overlap between consecutive blocks is used.

Three iterations of local corrections are carried out for each block in the present example and azimuth shifts, i.e., corresponding Doppler rate errors, are accumulated. Despite the relatively large block size, $1.2\,\%$ of the blocks provided erroneous measurements that do not converge throughout the iterations or exhibit invalid shift values. The estimates from those blocks are discarded and not shown in the results of Figure 15. In Figure 15b the resulting map of accumulated azimuth shifts is shown. It is evident, that the measurement undoubtedly replicates the physical appearance of the ice sheet. The rocky terrain with scattered snow fields on the left-hand side leads to almost no shifts, whereas the area spanned by the ice sheet results in varying negative shifts. The dark areas in the amplitude image, dominated by surface scattering, provide mainly small shifts. Overall, shift magnitudes are increasing towards the right-hand side. Measured azimuth shifts, i.e., corresponding Doppler rate errors, are inverted to depth estimates of the scattering scene within the glacial volume, where the refractive index is chosen as $n_{\text{ice}} = \sqrt{3.1}$ corresponding to almost solid ice. For each block, the inversion model in (12) requires estimates of the sensor altitude with respect to a tangential plane at the point where the echos impinge on the surface and the local incidence angle on the surface with respect to the surface normal. This information is provided from the X-band DEM in X-band and from the geocoding process during the P-band SAR data processing. Local incidence angles, used in the inversion, are averaged over the block and depicted in Figure 15c. The final depth inversion is displayed in Figure 15d, showing penetration depths down to $-84\,\mathrm{m}$. The general appearance replicates that of the azimuth shifts. Note the slight dependence with the incidence angle if comparing the color scale of Figure 15b and 15d, especially noticeable in far-range. The residual estimate after all corrective iterations in the map-drift approach is shown in Figure 15e. It provides a fair estimate of the possibly present measurement noise. Obviously, the error is lower for less penetration, i.e., smaller azimuth shifts. Overall, it does not exceed $4.5\,\mathrm{m}$ in the present scene and the mean error amounts to $0.52\,\mathrm{m}$.

### C. Validation with Tomograms

Due to the availability of tomographic acquisitions of the analyzed scene, we have conducted a qualitative validation of the single-image approach. The multi-baseline acquisitions in P-band are co-registered and tomographic processing is performed using all available baselines and a Capon beamformer for focusing in elevation dimension. Multi-looking with a 2048 x 256 window (azimuth x range) is performed to increase correlation with the block-wise map-drift measurement of equivalent size. Tomographic focusing is performed assuming free space propagation. The tomographic products represent 3-D images of the scattering glacial volume. Figure 16 shows three vertical slices along azimuth of the glacial volume together with the overlaid depth estimates of the single-image approach. The tomograms are registered to the acquired X-band DEM, so that the zero position of the vertical coordinate $z$ corresponds to the surface and negative values indicate the subsurface. Furthermore, an amplitude normalization along $z$ for every azimuth sample is performed to enhance the interpretability of the backscatter distribution. To account for the reduced propagation velocity in the ice sheet and refraction on the surface, a geometric correction is applied according to the relations given in [14], using the corresponding local

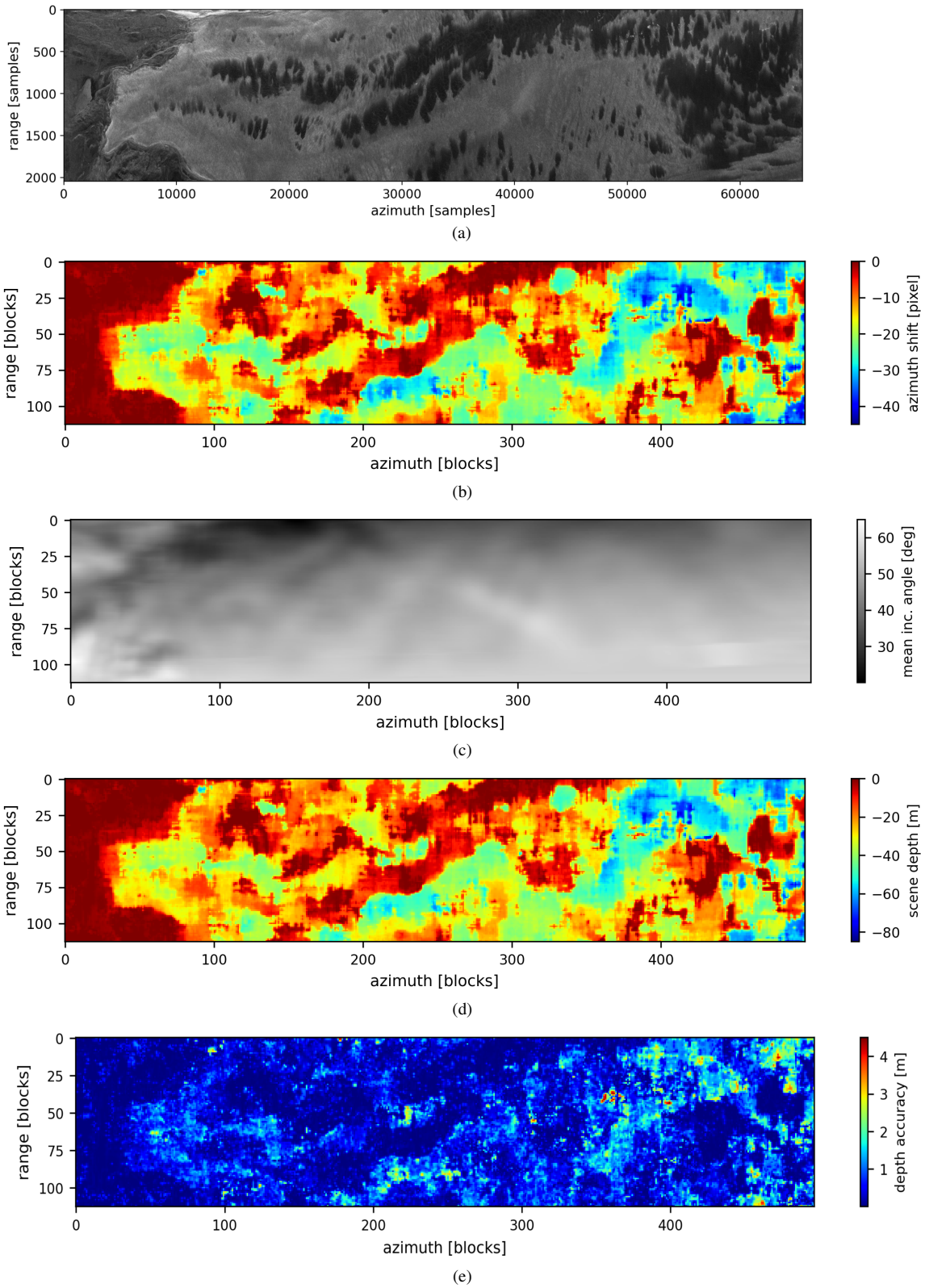


Fig. 15. Depth inversion results using the new single SAR image inversion approach on a scene from the K-transect in South-West Greenland showing: (a) amplitude image of the scene in HV polarization; (b) estimated azimuth shifts accumulated over three iterations of the local map-drift approach; (c) local incidence angles averaged in each block; (d) estimated scattering depth; (e) accuracy of depth estimate derived from residual Doppler rate error estimate after the last iteration of the local map-drift algorithm.

incidence angles and the same refractive index as used for the single-image approach, i.e., $n_{\text{ice}} = \sqrt{3.1}$. Overlaying the tomograms, the corresponding depth estimates using the single-image approach are plotted as red dots. The tomograms

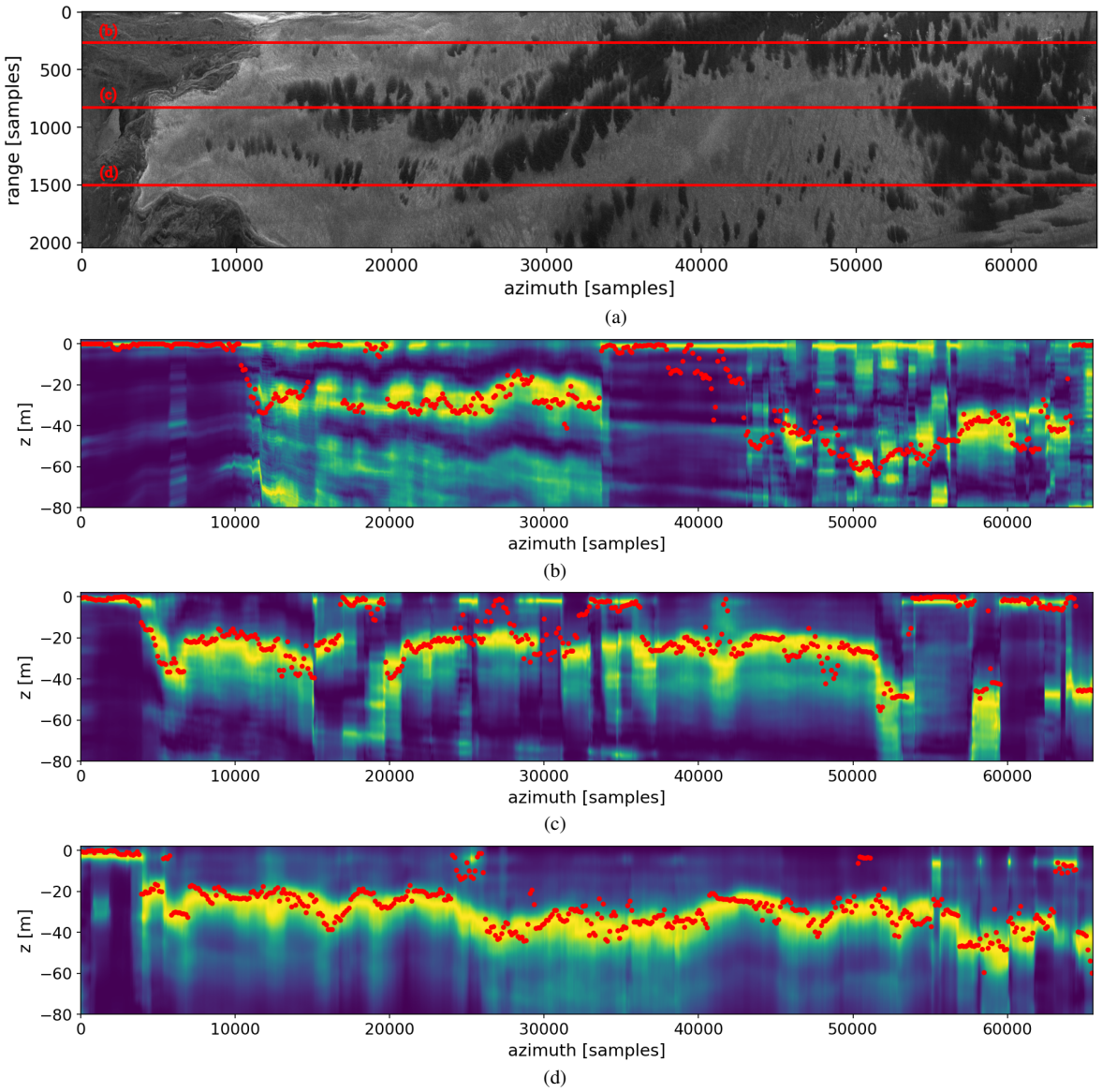


Fig. 16. Tomographic validation of the new single SAR image inversion approach showing three tomograms ((b) to (d)) through the whole azimuth extent of the scene (shown in (a)) along the red lines. The zero position of the $z$ coordinate is registered to the surface and negative $z$ values indicate the subsurface. Tomograms are normalized along $z$. Red dots indicate the depth estimate using the single-image approach.

are located at the range position coinciding with a block center. Note the overall good correspondence between the tomograms and the depth estimates using the single-image approach. Especially in areas where the backscatter is dominated by either a surface or distinct subsurface return, the agreement shows good consistency. Discrepancies mainly arise if multiple scattering sources at different depths are present (i.e., in Figure 16d around azimuth sample 25,000), leading to an averaging effect in the depth inversion, or if the depth of the dominant backscatter sources changes laterally fast (i.e. in Figure 16c from azimuth samples 25,000 to 35,000). The strong inconsistency in Figure 16b around sample 40,000 may be explained by the fact that nearby subsurface scene features within the range extent of the analyzed block influenced the map-drift measurement even if not visible in the strongly multi-looked tomograms. A similar argumentation may be used to explain other deviations in the two measurements. Note that high backscatter intensity does not necessarily imply good contrast, which controls the quality of the autofocus results. According to the concept for permittivity calibration introduced in Subsection IV-B, the refractive index of $n_{\text{ice}} = \sqrt{3.1}$ for both, the depth inversion using the single-image approach and the correction of the tomograms is chosen according to a visual calibration, by maximizing the apparent correlation between the measurements. The permittivity value fits remarkably well to the properties of solid ice in the ablation zone.

## VI. Conclusion and Discussion

Inspired by the difficulty of designing interferometric and tomographic SAR missions for planetary exploration, a strategy for the imaging of volumetric structures using low-frequency SAR images with moderate to good resolution has

been presented. The developed approach is based on an inversion procedure relying on single-image single-polarization SAR acquisitions to estimate volume parameters of ice sheets, namely, the penetration and the dielectric permittivity of the ice. It exploits phase errors present in the SAR image resulting from uncompensated non-linear propagation of the radar echos through ice.

As part of the single-image approach, a simple inversion model has been presented, allowing to link the phase errors to the depth of the scattering scene within an ice sheet, the average refractive index of the penetrated glacial volume, and the acquisition geometry. Based on the derived model it has been demonstrated that severe phase errors are to be expected in high-resolution SAR acquisitions of ice sheets, leading to strong defocusing of subsurface scenes. The phase errors can be effectively quantified and spatially resolved with the proposed local map-drift autofocus algorithm, from which penetration and permittivity estimates can be derived via the phase error model. Using high-resolution airborne P-band SAR data acquired over the Greenland ice sheet it has been demonstrated that the single-image approach delivers largely reliable penetration estimates when comparing them to tomographic products. The simplicity promotes the approach for SAR mission scenarios aimed at the exploration of planetary ice sheets such as the ice crust of Saturn's moon Enceladus or Jupiter's moon Europa. Furthermore, the potential capability of the single-image approach for calibrating the permittivity estimate for interferometric and tomographic acquisitions may be highly relevant for mitigating interferometric estimation biases over ice sheets in missions such as TanDEM-X or future missions such as Biomass and the Earth Explorer 10 candidate Harmony. A thorough assessment is left for future work.

The fact that the accuracy and reliability of the single-image approach is bounded by the map-drift shift estimation performance using a cross-correlation suggests that the approach may fail in highly homogeneous cryospheric scenes where not sufficient contrast is present. However, the analyzed scene comprises a wide spectrum of contrast level, promoting it as a suitable example for a variety of cryospheric scenes. The use of SAR acquisitions in cross-polarization is recommended to provide a higher sensitivity to subsurface features compared to acquisitions in co-polarization. Though, there is no general constraint on the polarization for the applicability of the single-image approach. The presented validation of the single-image approach using P-band SAR tomographic products provides a qualitative demonstration of its validity and potential. As part of future activities, further cryospheric F-SAR campaigns with the collection of ground measurements are planned. In particular, the measurements of local permittivity and the deployment of reference targets within boreholes in the ice sheet may support a consistent data-driven quantitative assessment of the accuracy and precision of the single-image approach.

Obviously, the proposed technique is not restricted to cryospheric applications but may be suitable for other semi-transparent natural media with significant permittivity difference to air, i.e., sand or soil. Furthermore, inverting atmospheric parameters from propagation induced phase errors may be achieved in similar manner.

## ACKNOWLEDGMENT

This study was financially supported by the German Space Agency at the German Aerospace Center (DLR) with funds from the German Federal Ministry for Economic Affairs and Energy (BMWi) under the project EnEx-AsGAr, registration no. 50NA1708. The Authors would like to thank M. Stelzig (LHFT, FAU) and Prof. M. Vossiek (LHFT, FAU) for their support in the EnEx project. They would also like to thank everyone involved in the ARCTIC15 campaign, which was conducted by DLR and ETH Zurich, Zurich, Switzerland. They would also like to give a special thanks to Dr. G. Fischer (DLR) for the valuable discussions and support with the F-SAR data.

## REFERENCES

[1] D. G. Vaughan *et al.*, "Observations: Cryosphere," in *Climate Change 2013: The Physical Science Basis. Contribution of Working Group I to the Fifth Assessment Report of the Intergovernmental Panel on Climate Change*, T. F. Stocker, D. Qin, G. K. Plattner, M. Tignor, S. K. Allen, J. Boschung, A. Nauels, Y. Xia, V. Bex, and P. M. Midgley, Eds. Cambridge, UK and New York, USA: Cambridge University Press, 2015.

[2] J. A. MacGregor *et al.*, "Radiostratigraphy and age structure of the Greenland ice sheet," *J. Geophys. Res. Earth Surf.*, vol. 120, no. 2, pp. 212–241, 2015.

[3] R. Orosei *et al.*, "Radar evidence of subglacial liquid water on Mars," *Science*, vol. 361, no. 6401, pp. 490–493, 2018.

[4] I. B. Smith, N. E. Putzig, J. W. Holt, and R. J. Phillips, "An ice age recorded in the polar deposits of Mars," *Science*, vol. 352, no. 6289, pp. 1075–1078, 2016.

[5] F. Heliere, C. Lin, H. Corr, and D. Vaughan, "Radio echo sounding of Pine Island Glacier, West Antarctica: Aperture synthesis processing and analysis of feasibility from space," *IEEE Transactions on Geoscience and Remote Sensing*, vol. 45, no. 8, pp. 2573–2582, 2007.

[6] J. J. Legarsky, S. P. Gogineni, and T. L. Akins, "Focused synthetic aperture radar processing of ice-sounder data collected over the Greenland ice sheet," *IEEE Transactions on Geoscience and Remote Sensing*, vol. 39, no. 10, pp. 2109–2117, 2001.

[7] S. Shabtaie and C. R. Bentley, "Ice-thickness map of the West Antarctic ice streams by radar sounding," *Annals of Glaciology*, vol. 11, p. 126–136, 1988.

[8] R. Jordan *et al.*, "The Mars express MARSIS sounder instrument," *Planetary and Space Science*, vol. 57, no. 14, pp. 1975 – 1986, 2009.

[9] R. Seu *et al.*, "SHARAD sounding radar on the Mars Reconnaissance Orbiter," *Journal of Geophysical Research: Planets*, vol. 112, no. E5, 2007.

[10] E. Weber Hoen and H. A. Zebker, "Penetration depths inferred from interferometric volume decorrelation observed over the Greenland Ice Sheet," *IEEE Transactions on Geoscience and Remote Sensing*, vol. 38, no. 6, pp. 2571–2583, 2000.

[11] J. J. Sharma, I. Hajnsek, K. P. Papathanassiou, and A. Moreira, "Estimation of glacier ice extinction using long-wavelength airborne Pol-InSAR," *IEEE Transactions on Geoscience and Remote Sensing*, vol. 51, no. 6, pp. 3715–3732, 2013.

[12] G. Parrella, I. Hajnsek, and K. P. Papathanassiou, "Polarimetric decomposition of L-band PolSAR backscattering over the Austfonna Ice Cap," *IEEE Transactions on Geoscience and Remote Sensing*, vol. 54, no. 3, pp. 1267–1281, 2016.

[13] S. Tebaldini, T. Nagler, H. Rott, and A. Heilig, "Imaging the internal structure of an Alpine glacier via L-band airborne SAR tomography," *IEEE Transactions on Geoscience and Remote Sensing*, vol. 54, no. 12, pp. 7197–7209, 2016.

[14] F. Banda, J. Dall, and S. Tebaldini, "Single and multipolarimetric P-band SAR tomography of subsurface ice structure," *IEEE Transactions on Geoscience and Remote Sensing*, vol. 54, no. 5, pp. 2832–2845, 2016.

[15] M. Pardini, G. Parrella, G. Fischer, and K. Papathanassiou, "A multi-frequency SAR tomographic characterization of sub-surface ice volumes," in *Proceedings of EUSAR 2016: 11th European Conference on Synthetic Aperture Radar*, 2016, pp. 1–6.

[16] W. Carrara, R. Goodman, and R. Majewski, *Spotlight Synthetic Aperture Radar: Signal Processing Algorithms*, ser. Artech House remote sensing library. Artech House, 1995.

[17] D. E. Wahl, P. H. Eichel, D. C. Ghiglia, and C. V. Jakowatz, "Phase gradient autofocus-a robust tool for high resolution SAR phase correction," *IEEE Transactions on Aerospace and Electronic Systems*, vol. 30, no. 3, pp. 827–835, 1994.

[18] O. O. Bezvesilniy, I. M. Gorovyi, and D. M. Vavriv, "Estimation of phase errors in SAR data by local-quadratic map-drift autofocus," in *2012 13th International Radar Symposium*, 2012, pp. 376–381.

[19] D. P. Belcher, "Theoretical limits on SAR imposed by the ionosphere," *IET Radar, Sonar Navigation*, vol. 2, no. 6, pp. 435–448, 2008.

[20] Z. Li, S. Quegan, J. Chen, and N. C. Rogers, "Performance analysis of phase gradient autofocus for compensating ionospheric phase scintillation in BIOMASS P-band SAR data," *IEEE Geoscience and Remote Sensing Letters*, vol. 12, no. 6, pp. 1367–1371, 2015.

[21] A. Benedikter, M. R. Cassola, G. Krieger, R. Scheiber, G. M. del Campo Becerra, R. Horn, M. Stelzig, A. Moreira, and M. Vossiek, "Potential of a multimodal orbital radar mission for the exploration of Enceladus," in *EGU General Assembly 2020, Online*, Mai.

[22] J. J. Sharma, I. Hajnsek, K. P. Papathanassiou, and A. Moreira, "Estimation of glacier ice extinction using long-wavelength airborne Pol-InSAR," *IEEE Transactions on Geoscience and Remote Sensing*, vol. 51, no. 6, pp. 3715–3732, 2013.

[23] F. Ulaby, M. C. Dobson, and J. L. Álvarez Pérez, *Handbook of Radar Scattering Statistics for Terrain*. Artech, 2019.

[24] M. Born *et al.*, *Principles of Optics: Electromagnetic Theory of Propagation, Interference and Diffraction of Light*, 7th ed. Cambridge University Press, 1999.

[25] C. Mätzler, "Improved Born approximation for scattering of radiation in a granular medium," *Journal of Applied Physics*, vol. 83, no. 11, pp. 6111–6117, 1998.

[26] C. Mätzler and U. Wegmüller, "Dielectric properties of freshwater ice at microwave frequencies," *Journal of Physics D: Applied Physics*, vol. 20, no. 12, pp. 1623–1630, dec 1987.

[27] A. Kovacs, A. J. Gow, and R. M. Morey, "The in-situ dielectric constant of polar firn revisited," *Cold Regions Science and Technology*, vol. 23, no. 3, pp. 245 – 256, 1995.

[28] J. C. Curlander and R. N. McDonough, *Synthetic Aperture Radar: Systems and Signal Processing*. Wiley-Interscience, 1991.

[29] G. Glaeser and H. Schröcker, "Reflections on refractions," *Journal for Geometry and Graphics*, vol. 4, no. 1, pp. 1–18, 2000.

[30] A. Benedikter and M. Rodriguez-Cassola, "A volumetric P-band imaging concept for the SAR exploration of Saturn's moon Enceladus," in *Proceedings of EUSAR 2021: 13th European Conference on Synthetic Aperture Radar*, 2016, pp. 1–6.

[31] F. Li, D. N. Held, J. C. Curlander, and C. Wu, "Doppler parameter estimation for spaceborne synthetic-aperture radars," *IEEE Transactions on Geoscience and Remote Sensing*, vol. GE-23, no. 1, pp. 47–56, 1985.

[32] R. Horn, A. Nottensteiner, and R. Scheiber, "F-SAR - DLR's advanced airborne SAR system onboard DO228," in *7th European Conference on Synthetic Aperture Radar*, 2008, pp. 1–4.

[33] G. Parrella, G. Fischer, I. Hajnsek, and K. P. Papathanassiou, "Mapping the ice zones of West Greenland using multi-frequency polarimetric SAR data," in *EUSAR 2018; 12th European Conference on Synthetic Aperture Radar*, 2018, pp. 1–6.

[34] G. Parrella, G. Fischer, M. Pardini, K. Papathanassiou, and I. Hajnsek, "Interpretation of polarimetric and tomographic signatures from glacier subsurface: the K-Transect case study," in *IGARSS 2019 - 2019 IEEE International Geoscience and Remote Sensing Symposium*, 2019, pp. 4927–4930.